AIAA JOURNAL
Vol. 32, No. 9, September 1994

Comparison of Coordinate-Invariant and Coordinate-Aligned Upwinding for the Euler Equations

Peter M. Hartwich*
ViGYAN, Inc., Hampton, Virginia 23666

A floating-shock fitting method for the Euler equations has been developed that uses one-sided spatial differences along and across streamlines. The coordinate-invariant formulation of the spatial differences permits automatic capture of shears. Results are presented for unsteady shocked flow in a duct with a ramp, for supercritical flow over a circular cylinder, and for subsonic, transonic, and supersonic ($0.3 \leq M_\infty \leq 1.5$) flow over airfoils. In flows with strong shears, the coordinate-invariant differencing concept appears to yield some gains in accuracy over Euler methods that rely on coordinate-aligned differencing concepts. In applications to transonic airfoils, fitted shocks have a tendency to be predicted upstream of captured shocks, regardless of whether coordinate-invariant or coordinate-aligned differencing is used. The coordinate-invariant differencing method requires between 2 and 3.5 times as much computing time as its coordinate-aligned counterpart.

I. Introduction

IT has become a widely accepted practice to construct upwind schemes for the multidimensional Euler equations with the convenient, albeit unlikely, assumption that flow and wave fronts (such as shocks and contacts) are aligned with grid lines (e.g., Refs. 1–4). This assumption makes it possible to immediately apply proven upwind techniques that have been devised for one-dimensional flow where wave fronts are always normal to the only spatial (or flow) direction. Although originally mostly aimed at mimicking the physics of inviscid flow for achieving flowfield results of improved accuracy, these one-dimensional upwinding concepts are being stripped of their physical justification when applied in a dimensionally split fashion to computations of multidimensional flow. There, their use is primarily justified by their userfriendliness: upwinding "naturally" introduces numerical damping that alleviates the need to add and fine tune artificial dissipation as in central-difference schemes.

Attempts to develop upwind schemes for the Euler equations that account for the actual orientation of flow features such as shears, sonic lines, and shocks can be categorized into methods that use some one-dimensional upwinding concept in a locally rotated reference frame,[5–7] that require a multidimensional flux function,[8–10] or a general shock-fitting methodology.[11] By conceptually ignoring shears, the first approach is the simplest one; still, it proved effective in applications to simple flows with straight shock fronts. The second concept accounts for shears and has produced some promising results for flows with nonsimple (e.g., curved) shocks.

This paper belongs in the third category. An Euler solver is presented that captures shears by solving the governing equations as if they were written in a streamline and normal coordinate system and that fits shocks; that is, the solution across shocks, which are allowed to freely float over the mesh, is updated using a refined version of the floating-shock fitting technique in Ref. 12. The purpose of this report is to assess the effectiveness of this technique by benchmarking it with reference solutions obtained with Euler solvers that rely on coordinate-aligned differencing and, where feasible, with experimental data.

Details of the formulation of the coordinate-invariant upwind Euler solver are given in the next five sections. The resulting method has been tested in simulations of complex interactions between shocks and shears as they occur in unsteady shocked flow in a duct with a ramp. Simulations of external flows with shocks of nonuniform strength, which produce rotational wakes, helped to determine whether the shear-capturing property of the present solver translates into more accurate flowfield results. These test cases included supercritical flow over a cylinder with inviscid separation and simulations of subsonic, transonic, and supersonic flows past a NACA 0012 airfoil.

II. Governing Equations

Upwind methods for the Euler equations are based on the theory of characteristics. Information about characteristic behavior becomes useful along the perimeter of the integration domain, along discontinuities, and in regions of supersonic flow where it suppresses the physically incorrect upstream propagation of signals. A nonconservative formulation of the governing equations allows choosing the dependent variables for promoting efficiency and accuracy of an upwind scheme for shock-free flows rather than for their suitability for a conservative "shock-capturing" formulation.[11–13] For instance, any upwind scheme requires information regarding the convective speed and the speed of sound to determine the direction of signal propagation. This points to an almost "natural" choice of the speed of sound and the convective speed, expressed in its components with respect to some reference frame, as dependent variables. Completing the set of dependent variables with entropy simplifies the set of governing equations (the complex energy equation gets reduced to a simple convection equation for entropy), and it decouples, as it should, the equation for energy from the equations for mass and momentum for homentropic flow; this can benefit the accuracy of the computed flowfield results.[14]

Another issue in formulating the governing equations is the choice of the independent variables. Arranging the governing equations as if they were written in a linearized (to avoid source terms stemming from centrifugal and centripetal force terms) streamline and normal coordinate system yields a form of the Euler equations that automatically captures shears. There are several options for implementing such a coordinate transformation.[11,15] The present formulation adopts Jameson's "rotated" differences[15] because his differencing concept permits time integration via a method of lines and because it makes for an easy transformation from stream-aligned to body-fitted coordinates.

After these preliminaries, the two-dimensional, compressible, nonconservative Euler equations in a linearized streamline and normal coordinate system are written as

$$\boldsymbol{Q}'_t + \boldsymbol{A}\boldsymbol{Q}'_{s'} + \boldsymbol{B}\boldsymbol{Q}'_{n'} = 0 \tag{1}$$

Received May 1, 1993; presented as Paper 93-3306 at the AIAA 11th Computational Fluid Dynamics Conference, Orlando, FL, July 6–9, 1993; revision received March 29, 1994; accepted for publication April 1, 1994.

*Research Scientist, 30 Research Drive. Member AIAA.

with

$$\boldsymbol{Q}' = (a, u', v', S)^T$$

where a is the speed of sound, u' the velocity component in flow direction, v' the velocity component normal to flow direction, and S the entropy. While on the streamline, $q = \sqrt{(u')^2 + (v')^2} = u'$ with q = convective speed, the velocity component v' is retained in Eq. (1) because its derivatives are generally nonzero. All quantities are normalized with reference values for pressure, density, and length (p_{ref}, ρ_{ref}, and l_{ref}, respectively). For a polytropic gas at constant γ (ratio of specific heats), the reference velocity, temperature, and time are

$$q_{\text{ref}} = \sqrt{p_{\text{ref}}/\rho_{\text{ref}}} \qquad T_{\text{ref}} = p_{\text{ref}}/(R\rho_{\text{ref}})$$
$$t_{\text{ref}} = l_{\text{ref}}/q_{\text{ref}} \tag{2}$$

where R is the specific gas constant. The nondimensional entropy is defined as

$$S = \ln(p/\rho^{\gamma})/(2\gamma\delta) \tag{3}$$

where $\delta = (\gamma - 1)/2$.

The coefficient matrices A and B are defined as

$$A = \begin{pmatrix} q & a\delta & 0 & 0 \\ a/\delta & q & 0 & -a^2 \\ 0 & 0 & q & 0 \\ 0 & 0 & 0 & q \end{pmatrix} \tag{4}$$

$$B = \begin{pmatrix} 0 & 0 & a\delta & 0 \\ 0 & 0 & 0 & 0 \\ a/\delta & 0 & 0 & -a^2 \\ 0 & 0 & 0 & 0 \end{pmatrix} \tag{5}$$

The Jacobians A and B possess distinct sets of eigenvalues, namely,

$$\Lambda_A = \text{diag}(\lambda_1, \lambda_2, \lambda_2, \lambda_4)_A = \text{diag}(q - a, q, q, q + a)$$

and (6)

$$\Lambda_B = \text{diag}(\lambda_1, \lambda_2, \lambda_2, \lambda_4)_B = \text{diag}(-a, 0, 0, a)$$

where diag is the diagonal matrix.

The eigenvalues in Eq. (6) point to another advantage of writing the governing equations in coordinates along and across streamlines: the sign of the eigenvalue $(\lambda_1)_A$ changes at true sonic points and not at spurious sonic points due to a projection of the velocity field onto an arbitrary coordinate system before evaluation of the characteristic slopes (example: consider Cartesian velocity components u and v with $u^2 < a^2 < u^2 + v^2$).

Upon application of a similarity transformation, $A\boldsymbol{Q}'_{s'}$ can be written as

$$A\boldsymbol{Q}'_{s'} = \frac{\lambda_{1,A}}{2}\begin{pmatrix} \delta \\ -1 \\ 0 \\ 0 \end{pmatrix}\tilde{A}_1 + \frac{\lambda_{4,A}}{2}\begin{pmatrix} \delta \\ 1 \\ 0 \\ 0 \end{pmatrix}\tilde{A}_2 + \lambda_{2,A}\begin{pmatrix} 0 \\ 0 \\ 1 \\ 0 \end{pmatrix}\tilde{A}_3 + \lambda_{2,A}\begin{pmatrix} a\delta \\ 0 \\ 0 \\ 1 \end{pmatrix}\tilde{A}_4 \tag{7}$$

with

$$\tilde{A}_1 = a_{s'}/\delta - u'_{s'} - aS_{s'} \qquad \tilde{A}_3 = v'_{s'}$$
$$\tilde{A}_2 = a_{s'}/\delta + u'_{s'} - aS_{s'} \qquad \tilde{A}_4 = S_{s'} \tag{8}$$

Similarly,

$$B\boldsymbol{Q}'_{n'} = \frac{\lambda_{1,B}}{2}\begin{pmatrix} \delta \\ 0 \\ -1 \\ 0 \end{pmatrix}\tilde{B}_1 + \frac{\lambda_{4,B}}{2}\begin{pmatrix} \delta \\ 0 \\ 1 \\ 0 \end{pmatrix}\tilde{B}_2 \tag{9}$$

with

$$\tilde{B}_1 = a_{n'}/\delta - v'_{n'} - aS_{n'}$$
$$\tilde{B}_1 = a_{n'}/\delta + v'_{n'} - aS_{n'} \tag{10}$$

A comparison of Eq. (8) and Eq. (10) demonstrates how the shear-capturing quality of the formulation in Eq. (1) comes about: vorticity $\tilde{A}_3$ and changes in entropy $\tilde{A}_4$ are convected only along streamlines but ignored across streamlines. Changes in the extended Riemann variables $\tilde{A}_1$, $\tilde{A}_2$, $\tilde{B}_1$, and $\tilde{B}_2$ are transported by acoustic waves along and across streamlines, which is physically correct since they are continuous everywhere except across shocks. But there, solutions are obtained anyway from the exact Rankine-Hugoniot relations via a floating-shock fitting technique rather than from finite-difference approximations to Eq. (1).

With the direction cosines $\hat{u} = u/q$ and $\hat{v} = v/q$, $\boldsymbol{Q}'_{s'}$ and $\boldsymbol{Q}'_{n'}$ are expressed locally in terms of arbitrary curvilinear coordinates as

$$\boldsymbol{Q}'_{s'} = (\xi_x\hat{u} + \xi_y\hat{v})\,\boldsymbol{Q}'_{\xi} + (\eta_x\hat{u} + \eta_y\hat{v})\,\boldsymbol{Q}'_{\eta}$$
$$\boldsymbol{Q}'_{n'} = (\xi_y\hat{u} - \xi_x\hat{v})\,\boldsymbol{Q}'_{\xi} + (\eta_y\hat{u} - \eta_x\hat{v})\,\boldsymbol{Q}'_{\eta} \tag{11}$$

Inserting Eq. (11) into Eq. (1) yields

$$\boldsymbol{Q}'_t + (A\hat{U} + B\hat{U}^*)\,\boldsymbol{Q}'_{\xi} + (A\hat{V} + B\hat{V}^*)\,\boldsymbol{Q}'_{\eta} = 0 \tag{12}$$

where the coefficients in Eq. (11) have been compressed into the expressions $\hat{U}$, $\hat{V}$, $\hat{U}^*$, and $\hat{V}^*$, respectively. The coefficients $\hat{U}$ and $\hat{V}$ are normalized contravariant velocity components, and the coefficients $\hat{U}^*$ and $\hat{V}^*$ are perpendicular to $\hat{U}$ and $\hat{V}$, respectively.

III. Spatial Differencing

Working toward an upwind differencing of the spatial derivatives in Eq. (12), now the Jacobians in Eq. (12) are subjected to a similarity transformation, which permits rewriting Eq. (12) as

$$\boldsymbol{Q}'_t + \{[R(\Lambda\hat{U})^+L]_A - [R(\Lambda\hat{U})^-L]_A\}\,\boldsymbol{Q}'_{\xi}$$
$$+ \{[R(\Lambda\hat{U}^*)^+L]_B - [R(\Lambda\hat{U}^*)^-L]_B\}\,\boldsymbol{Q}'_{\xi}$$
$$+ \{[R(\Lambda\hat{V})^+L]_A - [R(\Lambda\hat{V})^-L]_A\}\,\boldsymbol{Q}'_{\eta}$$
$$+ \{[R(\Lambda\hat{V}^*)^+L]_B - [R(\Lambda\hat{V}^*)^-L]_B\}\,\boldsymbol{Q}'_{\eta} = 0 \tag{13}$$

where R and L are the right and left eigenvectors, and $(\Lambda\hat{U})^{\pm}$, $(\Lambda\hat{U}^*)^{\pm}$, $(\Lambda\hat{V})^{\pm}$, and $(\Lambda\hat{V}^*)^{\pm}$ are diagonal matrices formed with the respective positive and negative eigenvalues. After a transformation from physical to computational coordinates [i.e., $(\xi, \eta) \rightarrow (i, j)$] a semidiscrete finite difference approximation to Eq. (13) reads

$$\boldsymbol{Q}'_t + \{[R(\Lambda\hat{U})^+L]_A + [R(\Lambda\hat{U}^*)^+L]_B\}\,\Delta^-_{i-1/2}\boldsymbol{Q}'$$
$$- \{[R(\Lambda\hat{U})^-L]_A + [R(\Lambda\hat{U}^*)^-L]_B\}\,\Delta^+_{i+1/2}\boldsymbol{Q}'$$
$$+ \{[R(\Lambda\hat{V})^+L]_A + [R(\Lambda\hat{V}^*)^+L]_B\}\,\Delta^-_{j-1/2}\boldsymbol{Q}'$$
$$- \{[R(\Lambda\hat{V})^-L]_A + [R(\Lambda\hat{V}^*)^-L]_B\}\,\Delta^+_{j+1/2}\boldsymbol{Q}' = 0 \tag{14}$$

where $\boldsymbol{Q}'_i$ and the Jacobians are evaluated at nodes (i, j), and $\Delta^{\pm}_{i\pm1/2}\boldsymbol{Q}'$ and $\Delta^{\pm}_{j\pm1/2}\boldsymbol{Q}'$ are backward and forward differences of second-order accuracy in regions of shock-free flow. As in Ref. 12, differences across a shock at nodes bracketing a shock are suppressed by setting the pertinent eigenvalues to zero; differences across a shock at nodes once removed from a shock front are avoided by assigning first-order one-sided differences to the pertinent eigenvalues.

IV. Time Differencing

A time-implicit operator containing block-tridiagonal matrices for the two-dimensional Euler equations is given by

$$\Big[I+\tau\Big(\{[R(\Lambda\hat{U})^{+}L]_A+[R(\Lambda\hat{U}^*)^{+}L]_B\}\Delta_{i-1/2}$$
$$-\{[R(\Lambda\hat{U})^{-}L]_A+[R(\Lambda\hat{U}^*)^{-}L]_B\}\Delta_{i+1/2}$$
$$+\{[R(\Lambda\hat{V})^{+}L]_A+[R(\Lambda\hat{V}^*)^{+}L]_B\}\Delta_{j-1/2}$$
$$-\{[R(\Lambda\hat{V})^{-}L]_A+[R(\Lambda\hat{V}^*)^{-}L]_B\}\Delta_{j+1/2}\Big)\Big]^n\Delta(\boldsymbol{Q}')^n$$
$$=-\tau\cdot\mathrm{RES}[(\boldsymbol{Q}')^n] \tag{15}$$

where I is the identity matrix, τ is the time step, $\Delta_{i\pm1/2}$ and $\Delta_{j\pm1/2}$ are first-order-accurate one-sided spatial difference operators, $\Delta(\boldsymbol{Q}')^n=(\boldsymbol{Q}')^{n+1}-(\boldsymbol{Q}')^n$, and n denotes the time level. The algorithm is cast in delta form to compute steady-state solutions that are independent of the time step size. The residual $\mathrm{RES}[(\boldsymbol{Q}')^n]$ comprises the spatial differences in Eq. (14) evaluated at the nth time level.

With approximate factorization (AF), a standard noniterative solution algorithm[16] for Eq. (15) is written as

$$\Big[I+\tau\Big(\{[R(\Lambda\hat{U})^{+}L]_A+[R(\Lambda\hat{U}^*)^{+}L]_B\}\Delta_{i-1/2}$$
$$-\{[R(\Lambda\hat{U})^{-}L]_A+[R(\Lambda\hat{U}^*)^{-}L]_B\}\Delta_{i+1/2}\Big)\Big]^n\Delta(\boldsymbol{Q}')^n$$
$$=-\tau\cdot\mathrm{RES}[(\boldsymbol{Q}')^n] \tag{16a}$$

$$\Big[I+\tau\Big(\{[R(\Lambda\hat{V})^{+}L]_A+[R(\Lambda\hat{V}^*)^{+}L]_B\}\Delta_{j-1/2}$$
$$-\{[R(\Lambda\hat{V})^{-}L]_A+[R(\Lambda\hat{V}^*)^{-}L]_B\}\Delta_{j+1/2}\Big)\Big]^n\Delta\boldsymbol{Q}'$$
$$=\tilde{\boldsymbol{Q}} \tag{16b}$$

$$(\boldsymbol{Q}')^{n+1}=(\boldsymbol{Q}')^n+\Delta\boldsymbol{Q}' \tag{16c}$$

The time-implicit algorithm described in Eqs. (16) is applied throughout the integration domain, even across fitted shocks. There, the only modification is that, at nodes immediately to the high-pressure side of a shock, the time step τ is set to zero. This insures that the update of the solution via the Rankine-Hugoniot relations remains untouched.

Note that the matrices $[\ldots]^{\pm}_A$ and $[\ldots]^{\pm}_B$ as they occur in each operator in Eq. (16) do not commute. Thus, they cannot be simultaneously diagonalized, which precludes implementation of a computationally much more efficient diagonalized version of the AF algorithm. As shown by the results given later, this disadvantage along with a higher operations count for evaluating the spatial derivatives leads to a severe penalty in overall computing time for the coordinate-invariant differencing approach compared with the coordinate-aligned upwind scheme from Ref. 12.

V. Floating-Shock Fitting

The present floating-shock fitting technique is a refined version of its predecessor described in Ref. 12. Particularly in the areas of accuracy and userfriendliness great strides have been made. The sketch in Fig. 1 helps to explain some of these improvements. There, two grid nodes, A and B, bracket a shock, with B lying on the high-pressure side of the shock. As illustrated in Fig. 1, this suffices as input for computing the local shock orientation in velocity space without any geometric input. This is accomplished by observing that the shock normal runs parallel to the change in velocity across a shock but in the opposite direction. This can be mathematically expressed as

$$\boldsymbol{N}=\Delta\boldsymbol{w}/|\Delta\boldsymbol{w}|$$

where $\boldsymbol{N}=(N_1,N_2)^T$ and $\boldsymbol{w}=(u,v)^T$ (u and v are Cartesian velocity components) with

$$N_1=-(u_B-u_A)/\sqrt{(u_B-u_A)^2+(v_B-v_A)^2}$$
$$N_2=-(v_B-v_A)/\sqrt{(u_B-u_A)^2+(v_B-v_A)^2} \tag{17}$$

Previously,[12] the local shock orientation was determined from a local orthogonal reference frame that was to be constructed along and normal to a coordinate line, which in the example in Fig. 1 is a line with $\eta=$ const. This process was found to be sometimes overly grid sensitive, and although only being cumbersome in two dimensions, it would add substantial computational expenditure when extended to three dimensions (which requires the use of reciprocal basis vectors).

Having defined the shock normal, speed of sound, the Cartesian velocity components, and entropy at B are computed from the Rankine-Hugoniot relations

$$a_B=a_A\frac{\sqrt{\gamma M^2-\delta}\sqrt{1+\delta M^2}}{(1+\delta)|M|}$$
$$\boldsymbol{w}_B=\boldsymbol{w}_A+a_A\frac{M^2-1}{(1+\delta)|M|}\boldsymbol{N} \tag{18}$$
$$S_B=S_A+\left[\ln\frac{\gamma M^2-\delta}{1+\delta}-\gamma\ln\frac{(1+\delta)M^2}{1+\delta M^2}\right]/(2\delta\gamma)$$

Note that the present formulation of the Rankine-Hugoniot relations avoids an explicit calculation of the velocity components tangential to the local shock front, as it was formerly[12] required, despite their constancy across shocks. The symbol M in Eq. (18) is the relative shock Mach number:

$$\mathrm{sign}(a_i-a_{i-1})\,|M|=\frac{(N_1u_A+N_2v_A)-W}{a_A} \tag{19}$$

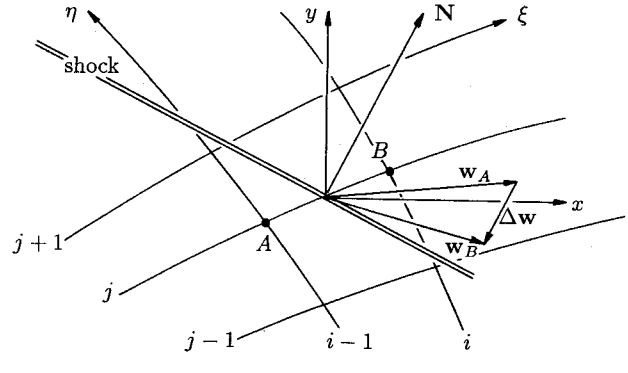

Fig. 1 Solution across a shock.

where W is the shock speed. The shock Mach number M is computed from an implicit relation first proposed by Moretti and DiPiano[17] for one-dimensional flow. Their concept is immediately applicable to the present floating-shock fitting procedure because the formulation in Eqs. (17–19) is quasi-one-dimensional, as it requires only knowledge about the orientation of the shock normal. Following Moretti and DiPiano, a shock parameter Σ is defined as

$$\Sigma = \frac{\sqrt{(\gamma M^2 - \delta)(1 + \delta M^2)} + \delta (M^2 - 1)}{(1 + \delta)|M|} \tag{20}$$

Upon inserting Eq. (18), Eq. (20) reduces to

$$\Sigma = \frac{a_B - \delta \boldsymbol{N} \cdot (\boldsymbol{w}_B - \boldsymbol{w}_A)}{a_A} \tag{21}$$

which is essentially a normalized difference of a Riemann variable (i.e., $a/\delta - \boldsymbol{N} \cdot w$) taken at the two nodes bracketing a shock. This Riemann variable makes for a sensitive, albeit not always reliable, shock detector since, in contrast to its counterpart, namely, $a/\delta + \boldsymbol{N} \cdot w$, it is discontinuous even across weak shocks [i.e., shocks with $M = \mathcal{O}(1)$].

The shock-fitting process is started by evaluating Eq. (21) for every possible pair of neighboring grid points. If Σ as computed from Eq. (21) exceeds some threshold $\Sigma_0 > 1$ and satisfies some other constraints, its value is used in a fixed-point iteration to determine the shock Mach number M as a solution to Eq. (20). As to additional constraints, the solution at node A, still assuming it designates the low-pressure side of a shock, is also required to satisfy the inequality

$$q_A^2 \geq |q_A| a_A \tag{22}$$

This makes sure that the flow on the low-pressure side is indeed supersonic unless it is an unsteady shock that runs into fluid at rest, as it happens in shock-tube problems. The constraint in Eq. (22) comes about because Σ as computed from Eq. (21) can exceed 1 with subsonic input from both nodes A and B. Furthermore, the cosine of the angle between the shock normal and the line segment between A and B

$$g = \frac{N_1(x_A - x_B) + N_2(y_A - y_B)}{\sqrt{(x_A - x_B)^2 + (y_A - y_B)^2}} \tag{23}$$

needs to be restricted to positive values. For negative g, Σ as computed from Eq. (21) is associated with an unphysical expansion shock rather than with a physically relevant recompression shock.

Another constraint on g is related to the local nature of the present floating-shock fitting technique that treats each shock fragment in any mesh interval independently from any other shock elements in neighboring mesh intervals. The advantage of such a heavily localized approach is that it eliminates the need for a cumbersome and computationally expensive organization of shock elements into a contiguous shock front, which can cause headaches when shock front bifurcations are encountered or when an extension of floating-shock fitting to three dimensions is considered. A drawback of this approach is that it can produce shock fronts that exhibit a peculiar sawtooth pattern that never gets smoothed out. This is avoided by requiring g to be always larger than the magnitude of the cosine of the angle between the line segment $\overline{AB}$ and each of the two diagonals of a computational cell circumscribed in Fig. 1 by the quadruple $(i-1, j-1)$, $(i, j-1)$, $(i, j+1)$, and $(i-1, j+1)$. This constraint preconditions the orientation of a shock fragment in any one mesh interval such that it is compatible with that of neighboring shock elements. This compatibility condition allows initially isolated shock fragments to eventually generate a smooth shock front.

All of these constraints possess the nice property that they are devoid of adjustable parameters, in contrast to the selection of a suitable threshold for Σ_0. If Σ_0 is set too low, the solution gets swamped with an exponentially growing number of shock points and breaks down. If Σ_0 is set too high, all shocks degenerate to isentropic recompressions. The desired solution between these extremes is found through experimentation. Extensive parameter studies indicate that it suffices to vary Σ_0 in increments of 0.01, and the values for Σ_0 that produced spatially and temporally converged flowfield results all lay in a range with $1.01 \leq \Sigma_0 \leq 1.05$, corresponding to a bandwidth of shock Mach numbers with $1.02 \leq M \leq 1.08$. Examples of appropriate choices for Σ_0 are given in Sec. VII.

Once a mesh interval bracketed by A and B is accepted as seat of a shock, and the solution on the high-pressure side is updated via the Rankine-Hugoniot relations, the solution at B is obtained from linear interpolation between actual location of the shock and a grid node once removed from the shock [i.e., the grid node at $(i+1, j)$ in Fig. 1]. The shock-fitting process is completed by moving the shock along the line segment $\overline{AB}$ by the increment

$$\Delta d = \Delta t \cdot W/g \tag{24}$$

The time step size Δt is to be determined with the constraint that the Courant-Friedrichs-Lewy (CFL) number is smaller than 1 to assure that the shock moves by at most one mesh interval per update. If a shock moves beyond B, the values at A are extended to B, and vice versa. Initially, a shock is assumed to be centered between A and B; at any time thereafter, its location is tracked by evaluating Eq. (24) at each shock update (i.e., at each time level n) and by accounting for its migration into mesh intervals neighboring that defined by A and B.

Depending on the relative orientation of shock wave and mesh lines, B might experience multiple updates. For uniform flow on the low-pressure side, all updates yield the same result (another advantage over the shock-fitting procedure in Ref. 12); for nonuniform flow on the low-pressure side, the last update is accepted. In the few occurrences of the latter case of multiple updates, the flowfield results were unaffected by the selection of the final update. Let this section be closed with the remark that the formal framework developed in Eqs. (17–24) also applies to shocks with the high-pressure side lying at A rather than B; just interchange the subscripts A and B.

VI. Boundary and Initial Conditions

For supersonic inflow, all variables are specified; supersonic outflow conditions are without effect on the flowfield solution. For subsonic inflow or outflow, the far-field boundary conditions determined from characteristic-based formulations as readily found in Ref. 18. Along solid walls, the Cartesian velocity components are updated by evaluating

$$\boldsymbol{w}_{\text{wall}} = \tilde{\boldsymbol{w}}_{\text{wall}} - \boldsymbol{n} W \tag{25}$$

where $\boldsymbol{n}$ is the outward-facing surface normal, and W is the contravariant velocity component orthogonal to the wall surface. The components in $\tilde{\boldsymbol{w}}_{\text{wall}}$ are computed from linear extrapolation from the interior of the integration domain, as is entropy. For flow cases involving a shock reflection off a solid wall, the speed of sound is updated using one-dimensional Riemann variables.[19] Otherwise, the speed of sound along a solid wall is iteratively calculated from the momentum equations by simplifying $\eta_x(\xi$ momentum$) + \eta_y(\eta$ momentum), which yields with the assumption of the wall coinciding with an η = const line

$$-\delta(\xi_x u + \xi_y v)(\eta_x u_\xi + \eta_y v_\xi) = (\xi_x \eta_x + \xi_y \eta_y) a a_\xi + (\eta_x^2 + \eta_y^2) a a_\eta \tag{26}$$

The boundary conditions along branch cuts are updated by averaging the extrapolates from the interior of the integration domain, and the calculations are always started from freestream.

VII. Results

Shocked Flow in a Duct

Montagné[20] proposed an unsteady flow problem that tests the capability of an Euler solver to simulate a rapid progression of

markedly dissimilar flow patterns involving regular and irregular shock reflections as well as interactions between shocks, expansion fans, and shears. In this problem, a flow in a two-dimensional channel, whose two sections of constant cross-sectional area are joined through a ramp of 20% slope (contraction ratio: 0.8), is started from uniform supersonic conditions ($M = 1.6$).

In Fig. 2, a computation with the floating-shock fitting method with coordinate-invariant upwinding is compared with Montagné's solution at the same physical time (the different callouts for the elapsed time are caused by dissimilar reference quantities). Both solutions are first-order accurate in time and use grids with 151 × 51 nodes. Montagné advanced his solution in global time

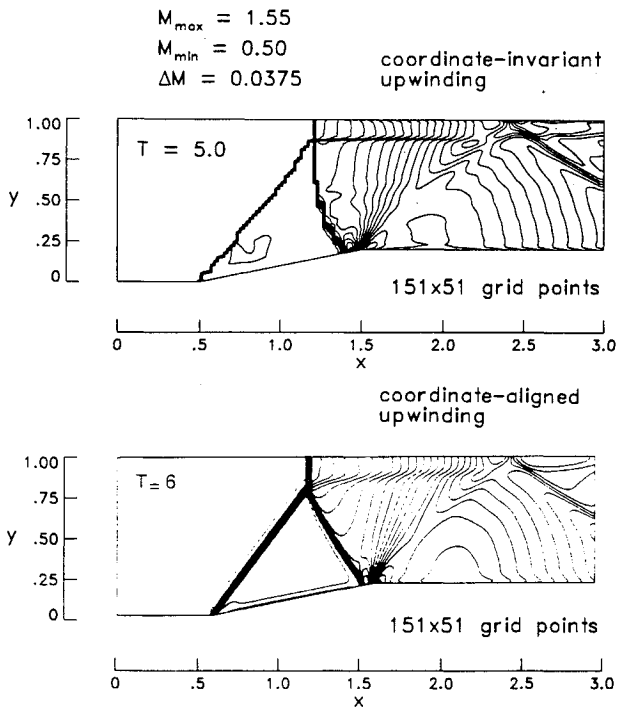

Fig. 2 Mach number distribution for unsteady flow in a duct—part 1 (bottom figure from Montagné [20]).

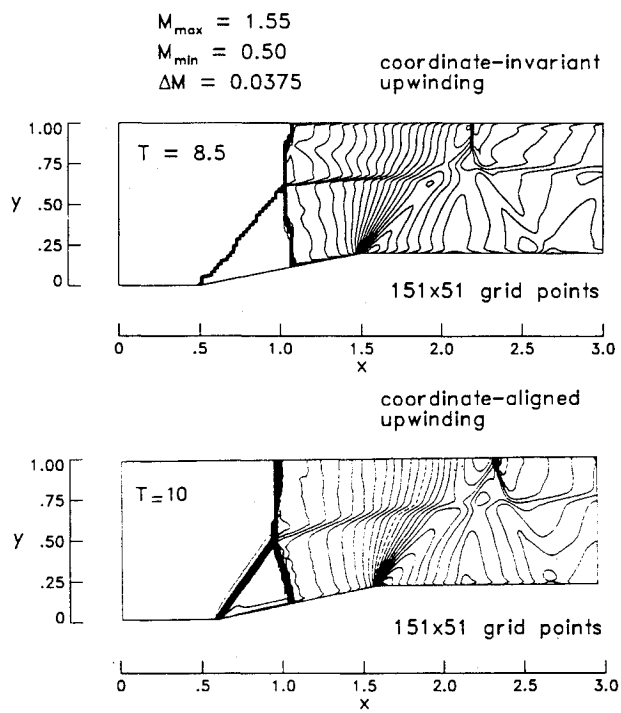

Fig. 3 Mach number distribution for unsteady flow in a duct—part 2 (bottom figure from Montagné[20]).

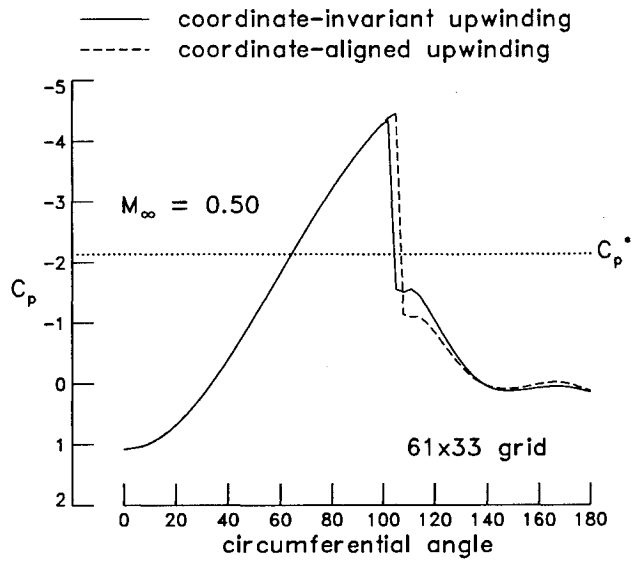

Fig. 4 Surface pressure distributions for supercritical flow over a circular cylinder.

steps with CFL = 0.8. The present solution is computed with constant time steps of $\tau = 0.02$, and shocks were fitted if the shock parameter Σ exceeded a threshold of $\Sigma_0 = 1.05$. For smaller values of Σ_0, the impinging shocks clung to the walls rather than being reflected; that is, multiple shock points developed along the walls with the shock normals describing sawtoothed shock fronts. Either plot of Mach number contours shows basically the same flow features. An oblique shock, anchored at the foot of the ramp, reflects irregularly off the ceiling of the duct, with a downward-running reflected shock hitting the ramp just upstream of a strong expansion fan that is centered at the head of the ramp. This expansion fan interacts with a shear that emanates from the triple-shock point and runs into the remnants of a regular shock reflection close to the outflow cross section.

Using the same layout as in Fig. 2, the comparison between the present coordinate-invariant upwind method and Montagné's coordinate-aligned upwind solver is repeated in Fig. 3 for a later point in physical time. Figure 3 shows that the Mach stem has grown in size and pushed the triple-shock point upstream. The shear, springing off the triple-shock point, runs down the duct first into the expansion fan, which is still rooted at the shoulder of the ramp, and eventually into a shock that has begun to form at the ceiling at about $x = 2.1$. Although it might be moot to dwell on the differences in the shapes of the contacts and in the shapes and strengths of the shocks in Figs. 2 and 3, it is fair to say that the coordinate-invariant upwinding with floating-shock fitting yields crisper representations of both shocks and shears than Montagné's shock-capturing method with coordinate-aligned upwinding.

Supercritical Flow over a Circular Cylinder

Salas was the first to discover that transonic inviscid flow over a circular cylinder admits separated flow as a valid solution to the Euler equations.[22] For flow with $M_\infty \geq 0.5$, a recompression shock forms on the leeside cylinder surface. The associated loss in total pressure causes the leeside stagnation point to move upstream. At the stagnation point, the vorticity generated across the shock gets shed into the flow. This vorticity bundles up into a shear layer that rolls up to form a recirculation bubble.

Figure 4 compares surface pressure signatures for supercritical flow ($M_\infty = 0.5$) over a circular cylinder as computed with the present coordinate-invariant upwind scheme with results obtained with the coordinate-aligned upwind method from Ref. 12. Both methods used the present shock-fitting technique with shocks being fitted if the shock parameter Σ exceeded a value of 1.04, which was found to be the minimum threshold for Σ_0 that still led to convergent computations. Either calculation was run for 3000

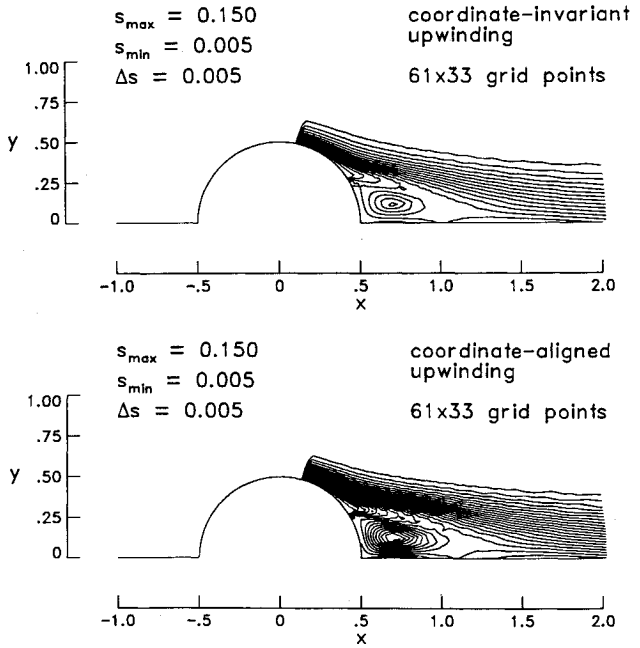

Fig. 5 Entropy contours for supercritical inviscid flow over a circular cylinder.

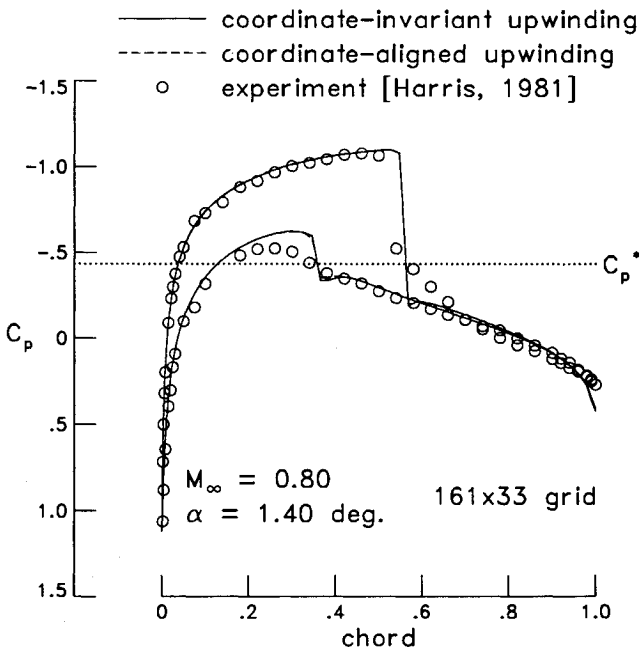

Fig. 6 Surface pressure distributions for a supercritical NACA 0012 airfoil.

cycles using local time stepping with CFL = 1.0. In both cases, the L_2 norm of all residuals was reduced by almost five orders of magnitude using 32-bit word arithmetic; the coordinate-aligned upwind method was more than twice as fast as its coordinate-invariant counterpart. The grid parameters such as grid extent (8 body diameters), grid density (61 × 33), and grid stretching lie within the specifications which defined the grids used in Salas' workshop.[22] The coordinate-invariant upwind differencing predicts a recompression shock that is located at 105 deg (measured from the windward stagnation point), 3 deg upstream of and considerably weaker than the shock in the result from the coordinate-aligned upwind method. Both surface pressure distributions indicate flow separation at a circumferential angle of about 140 deg and nonuniform surface pressure distributions in the recirculation region, with the coordinate-aligned upwind method predicting higher suction.

The entropy contours in Fig. 5 illustrate the flowfields associated with the surface pressure distributions in Fig. 4. In both cases, entropy is, as it should be, generated only across the recompression shocks. The stronger shock in the coordinate-aligned solution (more contours are emitted) produces a recirculation bubble with a much more pronounced vortical structure, which, in turn, generates a stronger suction on the leeward part of the cylinder. These differences in the flowfield characteristics are commensurably reflected by the respective drag coefficients that are $c_d = 0.06974$ for the coordinate-aligned solution and $c_d = 0.05892$ for the coordinate-invariant computation.

Transonic Airfoils

More practical examples of flows with rotational wakes downstream of nonuniform shocks are supercritical flows past airfoils. Figure 6 shows a comparison of surface pressures for a lifting NACA 0012 airfoil ($M_\infty = 0.8$ and $\alpha = 1.4$ deg) as computed with the present coordinate-invariant upwind scheme and with the coordinate-aligned upwind differencing from Ref. 12. Again, both methods use the present floating-shock fitting technique. For reference purposes, experimental data[23] are included as well, and if only to judge the discrepancies between experiment and numerical modeling. The angle of attack, which is not the incidence in the wind tunnel, reflects the effects of the tunnel walls that has been quantified using the analysis of Ref. 24, as suggested by Harris.[23] A far-field correction[19] accounting for the upwash effects of the lifting airfoil on the far-field solution has been used in the Euler simulations that were run on identical 161 × 33 C-type meshes, with 133 points lying on the airfoils surface. The radial extend was 6 chords, the maximum spacing of the first node off the surface was about 1% chord, and the radial stretching is characterized by a ratio of two consecutive radial mesh widths of about 1.1. These specifications lie well within the parameter spaces for typically employed Euler meshes. The shocks were fitted for the shock parameter Σ exceeding minimum values of 1.01 and 1.02 for the coordinate-invariant and for the coordinate-aligned method, respectively. These thresholds for Σ represent the respective minima for Σ_0 for which well-converged results were obtained for several subsonic values of M_∞, for several angles of attack, including nonlifting (α = 0.0 deg.) cases, and for mesh densities of 81 × 17, 161 × 33, and 321 × 65 nodes. The computed surface pressure signatures in Fig. 6 come to lie almost perfectly on top of each other, suggesting that the conceptual advantage of the coordinate-invariant method (i.e., the capture of the rotational wake) yields

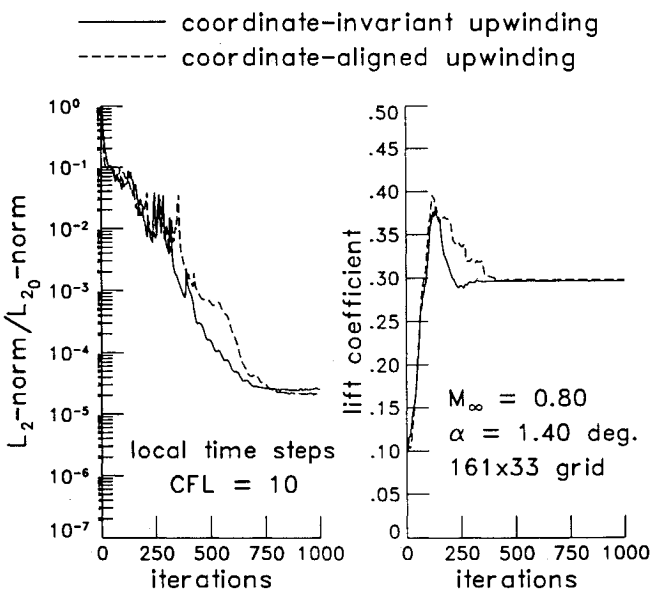

Fig. 7 Convergence summary for a supercritical NACA 0012 airfoil.

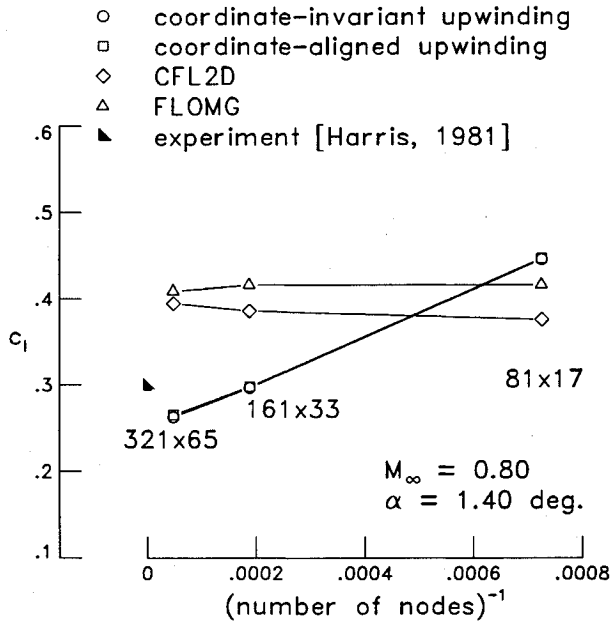

Fig. 8. Grid dependency of computed lift for a supercritical NACA 0012 profile.

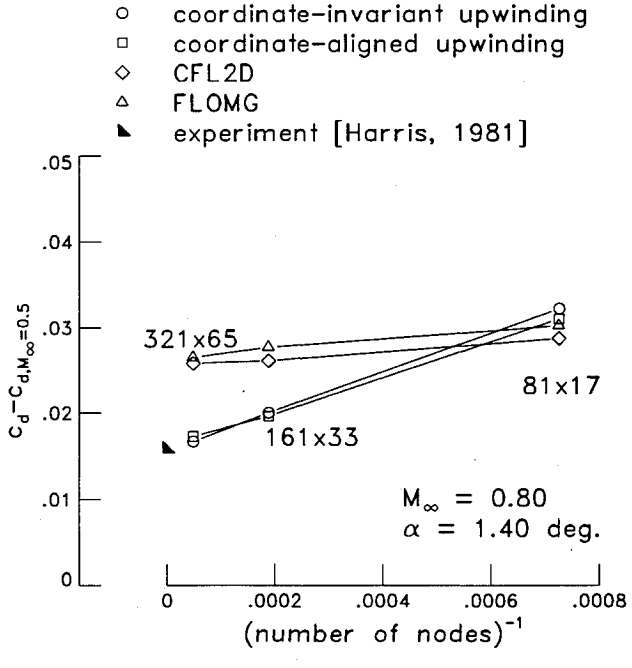

Fig. 9 Grid dependency of computed wave drag for a supercritical NACA 0012 profile.

only insignificant if any gains in accuracy compared with coordinate-aligned upwinding.

The convergence summaries in Fig. 7 for the computations in Fig. 6 give a flavor of what is meant with the preceding remark about well-converged answers. Contrary to frequent experiences with flow solvers that make an attempt to base upwinding on flow features rather than on grid orientation,[5,6,10] the solution computed with the coordinate-invariant upwinding converged as well as that with coordinate-aligned differencing. In either case, the L_2 norm of all residuals was reduced with about the same spectral radius (0.9860 vs 0.9867). The convergence performance in Fig. 7 was achieved using 32-bit word arithmetic, but this time on a more powerful workstation than in the previous simulations of supercritical flow past a cylinder. This let the disparity of the associated computing times grow: the coordinate-invariant upwind method required about 250% more computing time than the coordinate-aligned upwind scheme.

The variations of lift and drag with mesh density in Figs. 8 and 9 address the issue of spatial convergence of the results in Fig. 6. In these grid refinement studies only the grid density was varied without changing the grid stretching or the grid extent. Results are shown for the coordinate-invariant upwind method and for the coordinate-aligned upwinding from Ref. 12, with both these methods using the present floating-shock fitting technique. Also shown are results from Euler solutions with two established shock-capturing methods, namely, CFL2D (here used with Roe's flux-difference splitting and second-order one-sided differencing of the inviscid flux terms, see Refs. 2 and 25 for details) and FLOMG (as described in Ref. 26), which were run on the same meshes as the shock-fitting methods. The predominant result of these grid refinement studies is that the shock-capturing codes and the shock-fitting methods predict distinctly different asymptotic values for lift and wave drag. Surface pressure plots (not shown here) reveal that the fitted shocks on the two finer meshes come to lie upstream of the captured shocks. It should be noted that the fitted shocks move aft with increasing values of the threshold Σ_0, but even for values of Σ_0 as high as 1.05, the locations of the fitted shocks are predicted to be upstream of those of the captured shocks. Furthermore, it should also be pointed out that the present shock-fitting

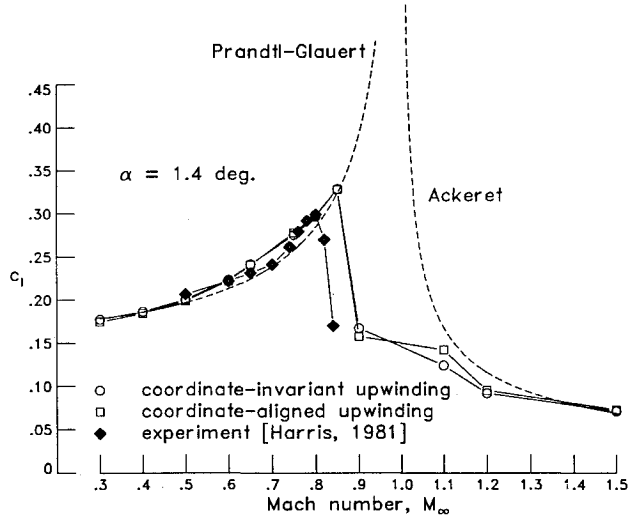

Fig. 10 Variation of lift with Mach number for a NACA 0012 profile.

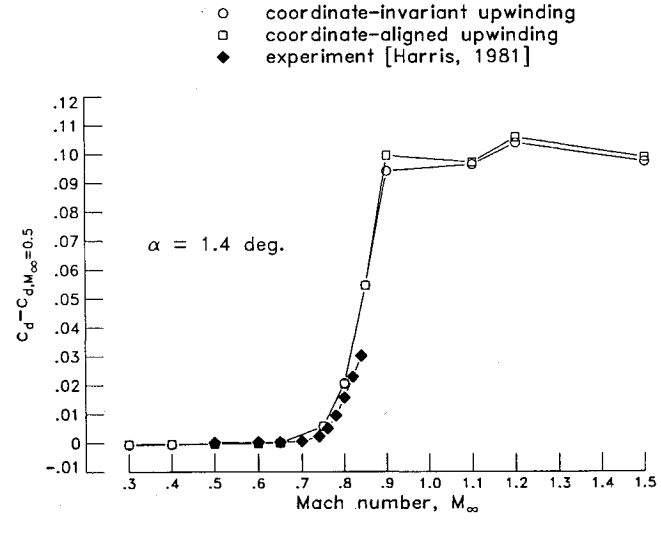

Fig. 11 Variation of wave drag with Mach number for a NACA 0012 profile.

results exhibit more grid sensitivity than in previous computations,[27] where the threshold Σ_0 was lowered as the meshes got coarser rather than being kept constant as in the present computations with floating-shock fitting.

When lift effects were eliminated from the supercritical case (i.e., $M_\infty = 0.8$ and $\alpha = 0.00$ deg), shock-capturing and shock-fitting results were in quite close agreement with each other as well as with experimental surface pressure data; this could be a consequence of the reduced strength of the recompression shocks compared with that of the upper-surface shock observed for the conditions used in Fig. 8. Repeating the mesh refinement study in Figs. 8 and 9 for subcritical flow ($M_\infty = 0.63$ and $\alpha = 2.00$ deg) demonstrated that any of the present shock-fitting schemes and FLOMG predicted asymptotic lift and drag (i.e., $c_d = 0$) in very close agreement. Additional grid refinement studies with both floating-shock fitting methods on O-type rather than C-type meshes for supercritical ($M_\infty = 0.800$) lifting ($\alpha = 1.40$ deg) as well as nonlifting flow past the NACA 0012 profile produced results very similar to those in Figs. 8 and 9. These results leave one with two possible explanations for the differences in the asymptotic values for lift and wave drag as predicted with the shock-fitting and the shock-capturing methods in Figs. 8 and 9: they are a consequence either of 1) some yet unidentified logical or coding mistake or of 2) the different treatment of the recompression shocks. Shock-capturing schemes determine the jump in entropy across shocks from some numerical dissipation scheme, whereas shock-fitting schemes predict the entropy production across shocks via the exact Rankine-Hugoniot relations.

The variations of lift and drag with freestream Mach number in Figs. 10 and 11 for a NACA 0012 airfoil at constant angle of attack ($\alpha = 1.40$ deg) illustrate the respective performances of the present coordinate-invariant differencing and of the coordinate-aligned upwinding from Ref. 12 over a wide speed range. Both schemes employ the present floating-shock fitting technique, with the threshold parameter Σ_0 kept at 1.01 and 1.02 for the coordinate-invariant and for the coordinate-aligned upwind scheme, respectively, for all freestream Mach numbers smaller than 1. For $M_\infty > 1$, both schemes invoked the shock-fitting procedures for $\Sigma > 1.05$. For subcritical flow ($M_\infty < 0.65$), both sets of computations, experimental data, and results from similarity agree quite well. For supersonic flow with $M_\infty > 1.4$, both Euler solutions are also in good agreement with similarity. This is a consequence of the trivial entropy distributions associated with these speed regimes. For subcritical flow, there are no shocks at all. Thus, entropy is constant throughout the integration domain. For supersonic flow, the shock system is composed of a bow shock just upstream of the airfoil nose with a very small subsonic pocket and by a pair of fishtail shocks anchored right at the trailing edge. Except for rather confined regions in the neighborhood of the airfoil, the curvature of these shocks is negligible, and, thus, for the most part the flow can be assumed as homentropic. In the transonic regime, both Euler solvers correctly pick up the transonic drag rise but overpredict maximum lift. For $0.9 < M_\infty < 1.1$, the flow becomes highly rotational, which leads to some differences in the predictions with the coordinate-invariant and the coordinate-aligned upwind scheme, which are, however, of little practical value due to the neglect of viscous shear fluxes in the mathematical model.

VIII. Conclusions

An extension of Jameson's concept of rotated differences for the full potential equation to the Euler equations has been implemented into a time-implicit floating-shock fitting method. The resulting technique has been used to assess the effectiveness of coordinate-invariant upwinding in comparison to coordinate-aligned differencing. Coordinate-invariant upwinding indeed appears to yield some gains in accuracy in flows with strong shears. Since these improvements in accuracy come at a steep extra computational expenditure, there is little reason to favor the coordinate-invariant approach in applications to two-dimensional flow where coordinate-aligned upwinding can easily compensate its disadvantage in accuracy by using finer meshes. However, this picture might change for three-dimensional flows, where relatively crude unadapted meshes are often dictated by limited computer memory.

Acknowledgments

This work was supported by NASA under Contract NASA-18585. The contributions by James M. Luckring of NASA Langley Research Center and by Mohammed M. Hafez of the University of California, Davis, in numerous discussions are gratefully acknowledged. Thanks are also due to Richard L. Campbell of NASA Langley Research Center, who provided the computations with the Euler/Navier-Stokes code FLOMG, and to James L. Thomas, also of NASA Langley Research Center, for doing the same with his CFL2D code.

References

[1]Chakravarthy, S. R., and Szema, K.-Y., "Euler Solver for Three-Dimensional Supersonic Flows with Subsonic Pockets," *Journal of Aircraft*, Vol. 24, No. 2, 1987, pp. 73–83.

[2]Vatsa, V. N., Thomas, J. L., and Wedan, B. W., "Navier-Stokes Computations of Prolate Spheroids at Angle of Attack," *Journal of Aircraft*, Vol. 26, No. 11, 1989, pp. 986–993.

[3]Frink, N. T., Parikh, P., and Pirzadeh, S., "A Fast Upwind Solver for the Euler Equations on Three-Dimensional Unstructured Meshes," AIAA Paper 91-0102, Jan. 1991.

[4]Chakravarthy, S. R., Szema, K.-Y., and Chen, C.-L., "A Universe-Series Code for Inviscid CFD with Space Shuttle Applications Using Unstructured Grids," AIAA Paper 91-3340, Sept. 1991.

[5]Davis, S. F., "A Rotationally Biased Upwind Difference Scheme for the Euler Equations," *Journal of Computational Physics*, Vol. 56, No. 1, 1984, pp. 65–92.

[6]Powell, K. G., and van Leer, B., "A Genuinely Multi-Dimensional Upwind Cell Vertex Scheme for the Euler Equations," AIAA Paper 89-0095, Jan. 1989.

[7]Dadone, A., and Grossman, B., "Characteristic-Based, Rotated Upwind Scheme for the Euler Equations," *AIAA Journal*, Vol. 30, No. 9, 1992, pp. 2219–2226.

[8]Roe, P. L., "Discrete Models for the Numerical Analysis of Time-Dependent Multidimensional Gas Dynamics," *Journal of Computational Physics*, Vol. 63, No. 2, 1986, pp. 458–476.

[9]Van Ransbeeck, P., Lacor, C., and Hirsch, C., "A Multidimensional Cell-Centered Upwind Algorithm Based on a Diagonalization of the Euler Equations," *Lecture Notes in Physics*, Vol. 371, Springer-Verlag, New York, 1990, pp. 238–242.

[10]Rumsey, C. L., van Leer, B., and Roe, P. L., "A Multi-Dimensional Flux Function with Applications to the Euler and Navier-Stokes Equations," *Journal of Computational Physics*, Vol. 105, No. 2, 1993, pp. 306–323.

[11]Verhoff, A., and O'Neil, P. J., "A Natural Formulation for the Numerical Solution of the Euler Equations," AIAA Paper 84-0163, Jan. 1984.

[12]Hartwich, P. M., "Fresh Look at Floating Shock Fitting," *AIAA Journal*, Vol. 29, No. 7, 1991, pp. 1084–1091.

[13]Chakravarthy, S. R., Anderson, D. A., and Salas, M. D., "The Split-Coefficient Matrix Method for Hyperbolic Systems of Gasdynamic Equations," AIAA Paper 80-0268, Jan. 1980.

[14]Hartwich, P. M., "Split Coefficient Matrix (SCM) Method with Floating Shock Fitting for Transonic Airfoils," *Lecture Notes in Physics*, Vol. 371, Springer-Verlag, New York, 1990, pp. 394–399.

[15]Jameson, A., "Iterative Solution of Transonic Flow over Airfoils and Wings, Including Flows at Mach 1," *Communications in Pure and Applied Mathematics*, Vol. 27, No. 3, 1974, pp. 283–309.

[16]Beam, R., and Warming, R. F., "An Implicit Finite-Difference Algorithm for Hyperbolic Systems in Conservation-Law-Form," *Journal of Computational Physics*, Vol. 22, No. 1, 1976, pp. 87–110.

[17]Moretti, G., and DiPiano, M. T., "An Improved Lambda-Scheme for One-Dimensional Flows," NASA CR 3712, Sept. 1983.

[18]Thomas, J. L., and Salas, M. D., "Farfield Boundary Conditions for Transonic Lifting Solutions to the Euler Equations," *AIAA Journal*, Vol. 24, No. 7, 1986, pp. 1074–1080.

[19]Chakravarthy, S. R., and Osher, S., "Numerical Experiments with the Osher Upwind Scheme for the Euler Equations," *AIAA Journal*, Vol. 21, No. 9, 1983, pp. 1241–1248.

[20]Montagné, J. L., "A Second-Order Accurate Flux Splitting Scheme in Two-Dimensional Gasdynamics," *Lecture Notes in Physics*, Vol. 218, Springer-Verlag, New York, 1985, pp. 406–411.

[21]Schmidt, W., Jameson, A., and Whitfield, D. L., "Finite-Volume Solutions to the Euler Equations in Transonic Flow," *Journal of Aircraft*, Vol. 20, No. 2, 1983, pp. 127–133.

[22]Salas, M. D., "Recent Developments in Transonic Euler Flow Over a Circular Cylinder," NASA TM 83282, April 1982; also *Mathematics and Computers in Simulation*, Vol. 25, No. 3, 1983, pp. 232–236.

[23]Harris, C. D., "Two-Dimensional Aerodynamic Characteristics of the NACA 0012 Airfoil in the Langley 8-Foot Transonic Pressure Tunnel," NASA TM 81927, April 1981.

[24]Barnwell, R. W., "Design and Performance Evaluation of Slotted Walls for Two-Dimensional Wind Tunnels," NASA TM 78648, Feb. 1978.

[25]Anderson, W. K., Thomas, J. L., and van Leer, B., "Comparison of Finite Volume Flux Vector Splittings for the Euler Equations," *AIAA Journal*, Vol. 24, No. 9, 1986, pp. 1453–1460.

[26]Maksymiuk, C. M., Swanson, R. C., and Pulliam, T. H., "A Comparison of Two Central Difference Schemes for Solving the Navier-Stokes Equations," NASA TM 102815, July 1990.

[27]Hartwich, P. M., "Comparison of Coordinate-Invariant and Coordinate-Aligned Upwinding for the Euler Equations," AIAA Paper 93-3306, July 1993.